九州工業大学学術機関リポジトリ
Kyutacar
Kyushu Institute of Technology Academic Repository

Drying-induced surface roughening of polymeric coating under periodic air blowing

Drying-induced Surface Roughening of Polymeric Coating under Periodic Air Blowing

Masato Yamamura, Tetsuro Uchinomiya, Yoshihide Mawatari and Hiroyuki Kage

Department of Applied Chemistry, Kyushu Institute of Technology

Sensui 1-1, Tobata, Kitakyushu, Fukuoka 804-8550 JAPAN

yamamura@che.kyutech.ac.jp

Key words: Drying, Liquid film coating, Marangoni flow, surface roughness, Modeling

ABSTRACT

We carried out numerical simulations of drying-induced surface roughening of a moving liquid layer under periodic air blowing conditions. Using spatially non-uniform Biot number profiles along the coating surface, the solutions of coupled diffusion/heat transfer equations reveal a periodic growth and relaxation in concentration gradients in the vicinity of the liquid-gas interface. The resultant interfacial stress variations promote particular asymmetric surface topographies that grow and level in a sequential manner. The unique surface roughness is identified by considering time scales required for the web motion, the stress-induced surface evolution, and the pressure-driven leveling. Predicted drying maps represent the surface roughening behavior as regions in parameter space.

INTRODUCTION

Liquid film coatings often respond to Marangoni stresses induced by a variation in surface tension. The stress pulls the liquid away from lower surface-tension regions and creates particular ridge(s)

and depression(s). For a given static surface tension gradient, the long-wave approximation [1] shows that the Marangoni stress gives a time scale for the surface deformation τ_m as linearly decreasing functions with respect to the film thickness and the surface tension difference. If the surface tension gradient relaxes, a capillary pressure and/or gravity can overcome the Marangoni forces and tend to level the film.

Air impingement dryer is a particular class of drying systems in which a coating responds to dynamic, rather than static, surface tension variations. When a liquid film on a moving web (substrate) is subject to air blowing from slit nozzles (Figure 1), local distributions in the solvent, and thus the surface tension, can change with a characteristic time scale of $\tau_w=2W/U$ where U and W denote the web speed and the half spacing between two neighboring nozzles, respectively. The coating surface evolves as would on a stationary substrate when the surface deformation rate is sufficiently fast compared to the web motion ($\tau_m \ll \tau_w$), while it would not deform in a finite time for $\tau_m \gg \tau_w$. In a particular intermediate case, the coating can respond to the periodic growth/relaxation of the interfacial stress, leading to show the stress-induced roughening and the pressure-driven leveling in a sequential manner. Furthermore, simultaneous heat and mass transfers across the gas/liquid interface strongly impact the stress development through its coupling with the local temperature and concentration. Thus we expect that moving coatings will exhibit rich responses in air impingement dryers.

2

Extensive numerical studies have been previously reported when a drying binary polymer coating

solidifies [2-6], crystallizes [7-8], gels [9], swells [10], or even exhibits skinning [11-12] but, to our knowledge,

not previously when a coating deforms via periodic, non-uniform interfacial stress distributions.

Indeed, most previous drying studies have assumed constant mass/heat transfer coefficients, and

hence uniform interfacial properties, for describing gas/liquid diffusions. The recent modeling [13]

deals with the film deformation over a traveling heat transfer coefficient, yet the solvent diffusion

was simply neglected. Despite the extensive studies for surface-tension-driven deformation of

viscous [14], colloidal [15] and polymeric [16-20] films, it has not yet been clarified how the drying coating

responds to non-static interfacial stresses. In this article, we present a mathematical model of coating

surface deformation by newly considering the periodic variations in interfacial properties via the

forced air blowing.

GOVERNING EQUATIONS

Drying model

Consider a thin liquid film of incompressible, nonreactive, Newtonian fluid coated on a moving

impermeable substrate of thickness b (Figure 2). The coating is in contact with a gas phase

unsaturated with the solvent vapor. The deformable air-liquid interface locates at $z = h (x, t)$ with

origin on the film-substrate interface where z and x are the Cartesian coordinates in the thickness and

3

the transverse directions, respectively. The fluid is a binary system of a volatile solvent (component 1) and a polymer (component 2) with no volume change on mixing. The upper gas-liquid interface is exposed to the blowing air with spatially non-uniform heat/mass transfer coefficients of $h^g(x)$ and $k^g(x)$, while the gas phase next to the lower substrate surface has a constant heat transfer coefficient h^G.

The governing equations are formulated based on previous drying studies [21-22]. Assuming the negligible transverse diffusion and no mass flux at the substrate-solution interface, we obtain the following expressions for the x- and z- components of the volume-averaged velocity as:

$$v_x^{\neq} = U .$$ (1)

$$v_z^{\neq} = 0 .$$ (2)

where U denotes the web speed in the x-direction.

Combining Eqs. (1)-(2) with the jump mass balance at the gas-solution interface[21] yields the expressions for the mass fluxes in the z-direction relative to the volume average velocity as:

$$z = \bar{h} : \quad j_1^{\neq} - \rho_1 \frac{d\bar{h}}{dt} = \frac{k^g M_1}{RT} \left(P_i - P_b \right).$$ (3)

$$z = \bar{h} : \quad j_2^{\neq} = \rho_2 \frac{d\bar{h}}{dt} .$$ (4)

where $j_i^{\neq}$ and ρ_i denote the mass flux and mass concentration of i-th component, $\bar{h}$ is the mean film thickness, t is the time, M_1 is the solvent molecular weight, P_i and P_b are the saturated solvent pressures at the interface and in the upper gas phase, R is the gas constant, and T is the absolute

temperature of the system. The right hand side of Eq. (3) represents the solvent evaporation from the gas-solution interface driven by the partial pressure difference.

The solvent and polymer fluxes satisfy:

$$j_1^{\neq} \hat{V}_1 + j_2^{\neq} \hat{V}_2 = 0. \tag{5}$$

where $\hat{V}_i$ is the partial specific volume of the i-th component. Substituting Eqs. (3)-(4) into Eq. (5) gives the position of the liquid-gas interface as;

$$z = \overline{h} \quad : \quad \frac{d\overline{h}}{dt} = -\hat{V}_1 \frac{k^g M_1}{RT}(P_i - P_b). \tag{6}$$

A no-flux boundary condition is imposed at the substrate-liquid interface because no solvent penetrates the substrate:

$$z = 0 \quad : \quad \frac{\partial \rho_1}{\partial z} = 0. \tag{7}$$

Initially, the solution layer is assumed to have a uniform composition and film thickness as:

$$t = 0 \quad : \quad \rho_1 = \rho_{10}, \quad h(x) = L. \tag{8}$$

Fick's law is used to describe the diffusive flux based on the volume average velocity as a reference frame. We assume that stress-induced transverse flows give negligible effect on concentration/temperature fields in the thickness direction, i.e., heat and mass transfers in the z-direction are fully de-coupled from the liquid motion. Thus the one-dimensional solvent continuity equation is expressed as

$$\frac{\partial \rho_1}{\partial t} = \frac{\partial}{\partial z}\left(D \frac{\partial \rho_1}{\partial z}\right). \tag{9}$$

5

where D is the concentration-dependent mutual diffusion coefficient.

The gas-liquid interface moves as the solvent evaporates. The following coordinate transformation is used to facilitate numerical treatment of the moving interface:

$$\eta \equiv \frac{z}{\bar{h}}.$$ (10)

The governing equation (9) is then re-written as:

$$\frac{\partial \rho_1}{\partial t} = \frac{\eta}{\bar{h}} \frac{d\bar{h}}{dt} \frac{\partial \rho_1}{\partial \eta} + \frac{1}{\bar{h}^2} \frac{\partial}{\partial \eta} \left(D \frac{\partial \rho_1}{\partial \eta} \right).$$ (11)

Integrating Eq. (11) from η=0 to 1 and using boundary conditions Eqs. (3), (6) and (7) give the expressions for the mean film thickness $\bar{h}$ and the residual solvent content $\bar{h}I$ as:

$$I(t) = \int_0^1 \rho_1 d\eta,$$ (12)

$$\bar{h} = \left(\frac{1 - \rho_{10} \hat{V}_1}{1 - I\hat{V}_1} \right) L,$$ (13)

$$\frac{d}{dt} \left(\bar{h} \cdot I \right) = -\frac{k^g M_1}{RT} \left(P_i - P_b \right).$$ (14)

Thus we explicitly obtain the mean thickness and the residual solvent level from Eqs. (13)- (14).

Assuming that the heat transfer resistance in the gas phase is much greater than the conductive resistances in the film and the substrate, the temperature $\bar{T}$ is uniform across the coating and given by:

$$\left(\rho C_p \bar{h} + \rho_s C_{ps} b \right) \frac{\partial \bar{T}}{\partial t} = -\frac{k^g M_1}{RT} (P_i - P_b) \Delta H - h^g (\bar{T} - T_b) - h^G (\bar{T} - T_b).$$ (15)

where ρ and ρ_s are densities of the solution and the substrate, C_p and C_{ps} are average heat capacities of the solution and substrate, ΔH is the latent heat of the solvent vaporization, and T_b the gas bulk

temperature. The first, second and third terms on the right hand side respectively denote the

evaporative heat loss, convective heat flux from the gas-solution interface, and that from the

gas-substrate interface. The initial temperature in the liquid and substrate phases is uniform at

$\bar{T} = T_0$.

Film equation

Now let us turn to the film evolution equation. The velocity distribution within the film is

defined as $u(x, z)$ with origin on the film substrate interface. The stress boundary condition for the

velocity at the free surface is given by:

$$z = h \quad : \quad \mu \frac{\partial u}{\partial z} = \frac{d\sigma}{dx} \, . \tag{16}$$

where μ and σ respectively denote the fluid viscosity and the surface tension. Here we assume

negligible shear stress in gas phase compared to the Marangoni stress. No slip boundary condition at

$z=0$ gives $u=0$.

Because the local thickness variation of interest is sufficiently small compared to the mean

thickness as $(h - \bar{h})/\bar{h} \ll 1$, use of the lubrication approximation is appropriate. Neglecting inertia

and gravity, the equations of motion in x and z directions are:

$$\frac{\partial p}{\partial x} = \mu \frac{\partial^2 u}{\partial z^2} \, , \tag{17}$$

$$\frac{\partial p}{\partial z} = 0 \, . \tag{18}$$

Thus the local liquid pressure p is independent of z. Substituting Eq. (16) into Eq. (17) and integrating the parabolic velocity profile in the z-direction gives the total flux Q at a given position x as

$$Q \equiv \int_0^h u\,dz = -\frac{h^3}{3\mu}\frac{\partial p}{\partial x} + \frac{h^2}{2\mu}\frac{d\sigma}{dx}. \qquad (19)$$

The mass conservation law gives:

$$\frac{\partial h}{\partial t} = -\frac{\partial Q}{\partial x} - \frac{\partial \overline{h}}{\partial t}. \qquad (20)$$

where the second term on the right hand side represents the mean film shrinkage rate due to the solvent evaporation and obtained from Eq. (6) with unit of velocity.

Considering a small topographic change in the surface profile, an approximate form for the free surface curvature yields,

$$p = -\sigma \frac{\partial^2 h}{\partial x^2}. \qquad (21)$$

where the static pressure due to the air impingement is neglected for simplicity.

Combining Eqs. (19)-(21) yields a non-linear evolution equation for the film thickness h as:

$$\frac{\partial h}{\partial t} = -\frac{\partial}{\partial x}\left[\frac{h^3}{3\mu}\frac{\partial}{\partial x}\left(\sigma\frac{\partial^2 h}{\partial x^2}\right) + \frac{h^2}{2\mu}\frac{\partial\sigma}{\partial x}\right] - \hat{V}_1 \frac{k^g M_1}{RT}\left(P_i - P_b\right). \qquad (22)$$

Note that Eq. (22) reduces Eq. (6) for the case when no transverse liquid motion takes place.

To numerically solve Eq (22), non-periodic boundary conditions were applied at the outer boundaries of the unit computational cell at $x=W$ and $-W$ as:

8

$$x = W : \quad \frac{\partial h}{\partial x} = \frac{\partial^2 h}{\partial x^2} = 0, \quad \frac{\partial \rho_1}{\partial x} = 0, \quad \frac{\partial \overline{T}}{\partial x} = 0, \tag{23}$$

$$x = -W : \quad \frac{\partial h}{\partial x} = \frac{\partial^2 h}{\partial x^2} = 0, \quad \frac{\partial \rho_1}{\partial x} = 0, \quad \frac{\partial \overline{T}}{\partial x} = 0. \tag{24}$$

Nondimensionalization

The continuity and the film equations are non-dimensionalized by introducing the following dimensionless variables:

$$c = \frac{\rho_1}{\rho_{10}}, \quad t^* = \frac{D_0 t}{L^2}, \quad x^* = \frac{x}{W}, \quad z^* = \frac{z}{L}, \quad h^* = \frac{h}{L}, \quad P^* = \frac{P}{P_0},$$

$$\Theta = \frac{\overline{T}}{T_0}, \quad \mu^* = \frac{\mu}{\mu_0}, \quad \sigma^* = \frac{\sigma}{\sigma_0}. \tag{25}$$

The dimensionless forms of the governing equations are:

$$\frac{\partial c}{\partial t^*} = \frac{\eta}{\overline{h}^*} \frac{d\overline{h}^*}{dt^*} \frac{\partial c}{\partial \eta} + \frac{1}{\overline{h}^{*2}} \frac{\partial}{\partial \eta}\left(\frac{D}{D_0} \frac{\partial c}{\partial \eta}\right), \tag{26}$$

$$\eta = 1 \quad : \quad -\left(\frac{D}{D_0}\right)\frac{1}{\overline{h}^*}\frac{\partial c}{\partial \eta} - c\frac{d\overline{h}^*}{dt^*} = Bi(P_i^* - P_b^*), \tag{27}$$

$$\eta = 1 \quad : \quad \frac{d\overline{h}^*}{dt^*} = -(\rho_{10}\hat{V}_1)Bi(P_i^* - P_b^*), \tag{28}$$

$$\eta = 0 \quad : \quad \frac{\partial c}{\partial \eta} = 0, \tag{29}$$

$$\left(\frac{\rho C_p \overline{h}^* + \rho_s C_{ps} b/L}{\rho_{10} C_p}\right)\frac{\partial \Theta}{\partial t^*} = -Bi(P_i^* - P_b^*)\left(\frac{\Delta H}{C_p T_0}\right) - Nu^g Le(\Theta - \Theta_b) - Nu^G Le(\Theta - \Theta_b), \tag{30}$$

$$\frac{\partial h^*}{\partial t^*} = -\frac{L^2/D_0}{\mu_0 W^4/(\sigma_0 L^3)}\frac{\partial}{\partial x^*}\left[-\frac{h^{*3}}{3\mu^*}\frac{\partial}{\partial x^*}\left(-\sigma^*\frac{\partial^2 h^*}{\partial x^{*2}}\right) + \frac{h^{*2}}{2\mu^*}\left(\frac{W}{L}\right)^2\frac{\partial \sigma^*}{\partial x^*}\right]$$

$$-\left(\rho_{10}\hat{V}_1\right)Bi\left(P_i^* - P_b^*\right), \tag{31}$$

$$x^* = 1: \quad \frac{\partial h^*}{\partial x^*} = \frac{\partial^2 h^*}{\partial x^{*2}} = 0, \quad \frac{\partial c}{\partial x^*} = 0, \quad \frac{\partial \Theta}{\partial x^*} = 0, \tag{32}$$

$$x^* = -1: \quad \frac{\partial h^*}{\partial x^*} = \frac{\partial^2 h^*}{\partial x^{*2}} = 0, \quad \frac{\partial c}{\partial x^*} = 0, \quad \frac{\partial \Theta}{\partial x^*} = 0, \tag{33}$$

$$t = 0 \quad : \quad c = 1, \quad \bar{h}^* = h^* = 1, \quad \Theta = 1. \tag{34}$$

The dimensionless groups arising from the analysis are

$$Bi = \frac{k^g L}{D_0 \rho_{10}} \cdot \frac{P_0 M_1}{RT}, \tag{35}$$

$$Nu^G = \frac{h^G L}{\lambda_0}, \tag{36}$$

$$Nu^g = \frac{h^g L}{\lambda_0}, \tag{37}$$

$$Le = \frac{\lambda_0}{\rho_0 C_p D_0}. \tag{38}$$

where λ_0 denotes the reference thermal conductivity, Biot number, B_i, is a measure of internal to

external mass transfer resistance, and the Lewis number, Le, is a measure of mass to heat transfer

resistance.

Drying parameters

The flow pattern of impinging jets can be subdivided into the stagnation region beneath the air

impinging point, and the wall jet region along the solid surface [23]. The heat transfer coefficients

corresponding to the two regimes have been correlated for a jet flow from a single slit nozzle onto a

stationary infinite plane [24]:

$$\frac{h^G B}{\lambda^G} = 0.06958 Re^{0.8} \Pr^{0.43} (\frac{x}{H})^{-0.37} (\frac{H}{B})^{-0.62}, \tag{39}$$

$$\frac{h^G B}{\lambda^G} = 1.42 Re^{0.58} \Pr^{0.43} (\frac{H}{B})^{-0.62}. \tag{40}$$

where λ^G denotes the gas thermal conductivity, H the nozzle height, and B the slit width. The Reynolds number, $Re = \rho^G u^G B / \mu^G$, and the Prandtl number, $Pr = \mu^G C_p^G / \lambda^G$, are defined with respect to the outflow air velocity, u^G, the gas density, ρ^G, the gas viscosity, μ^G, and the heat capacity of the gas, C_p^G. The cut-off value from Eq. (40) was used in the vicinity of the impinging point because the transfer coefficient in the wall jet region from Eq. (39) becomes infinite at x=0.

The mass transfer coefficients at the stagnation and the wall jet regions were readily obtained using the analogy between the heat and mass transfers as:

$$\frac{k^G B}{D^G} = 0.06958 Re^{0.8} Sc^{0.43} (\frac{x}{H})^{-0.37} (\frac{H}{B})^{-0.62}, \qquad (41)$$

$$\frac{k^G B}{D^G} = 1.42 Re^{0.58} Sc^{0.43} (\frac{H}{B})^{-0.62}. \qquad (42)$$

where D^G represents the diffusion coefficient in the gas phase, and $Sc = \mu^G / (\rho^G D^G)$ the Schmidt number. In the air impingement from nozzle arrays, the wall jets of adjacent nozzles can impinge upon each other and show a particular boundary layer separation [23]. In addition, the lateral air flow due to the web motion is capable of changing the local boundary layer thickness. In the present computations, we assume negligible effects of the web motion and the interactions from neighboring nozzles on the flow pattern and simply use Eqs. (39) -(42) to obtain the heat/mass transfer coefficients.

In order to simulate the drying behavior on a moving substrate, the Biot/Nusselt number profiles from Eqs. (39)-(42) were numerically moved at the same speed as, but in the opposite direction to,

the web motion. Periodic boundary condition was imposed for Biot/Nusselt numbers, thus the

calculation only needs to be performed in a unit computational cell with the length of 2W. The local

heat/mass transfer coefficients were updated at every step of $\Delta x/(U\Delta t)$ where Δt denotes the

integration time step and Δx the dimensional grid spacing in the x-direction. The time variations in

physical quantities at x=0 are monitored in order to depict their surface profiles along the moving

direction.

Closure of the model requires expressions for the material properties as functions of the

temperature and the mass concentration. Specifically, this article treats the drying of

poly(vinyl-alcohol)(PVA) /water solutions. A linear approximation for the surface tension with

respect to temperature and concentration gives:

$$\sigma - \sigma_0 = \sigma_T(\overline{T} - T_0) + \sigma_c(\rho_1 - \rho_0) \tag{43}$$

where T_0 , ρ_0 and σ_0 denote the reference temperature, solvent mass concentration and surface

tension. The surface tension gradients, σ_T and σ_C, are negative and positive constants in the

temperature/concentration ranges of interest. The resultant surface tension drops with decreasing the

solvent content because of the surface activity of PVA.

The solution viscosity is assumed to depend exponentially on the polymer mass fraction at the

gas-liquid interface and the temperature as:

$$\ln(\mu/\mu_0) = \gamma\left(m_\mu\omega_2 + \frac{n_\mu}{\overline{T}} + k_\mu\right). \tag{44}$$

where γ denotes the viscosity power-law index, ω_2 is the polymer mass fraction, μ_0 is the solvent

viscosity, and k_μ, m_μ, and n_μ are the material constants.

The Flory-Huggins equation is use to obtain the solvent partial pressure P_1 at the solution/gas

interface:

$$0.56 < \omega_2 \leq 1 \quad : \quad \frac{P_1}{P_1^*} = (\rho_1 \hat{V}_1) \exp \left\{ (1 - \rho_1 \hat{V}_1) + \chi_{12}(1 - \rho_1 \hat{V}_1)^2 \right\}, \tag{45}$$

$$0 \leq \omega_2 \leq 0.56 \quad : \quad \frac{P_1}{P_1^*} = 1. \tag{46}$$

where χ_{12} is the solvent-polymer interaction parameter. The saturated vapor pressure of solvent P_1^*

was calculated from the Antoine equation $\log P_1^* = A - B/(C + \bar{T})$ where the constant parameters A,

B, and C are available in the literature.

The temperature/concentration-dependent diffusion coefficient is commonly predicted using the

free-volume theory and the friction-based models [25]. In this article, we simply set the mutual

diffusion coefficient as an exponential function of polymer mass fraction being independent on

temperature of interest as

$$D = D_{10} \exp(-m_D \omega_2^{n_D}). \tag{47}$$

where D_{10} denotes a constant pre-exponential factor, and the exponents m_D and n_D determine how

strongly the diffusion coefficient depends on the polymer concentration.

The material parameters in Eqs. (45)-(47) were determined by fitting the calculated values with

experimental data available in the literature [26]. All of the drying parameters used in this analysis are

presented in Table 1.

Solution procedure

The set of coupled partial differential equations were discretized in space using an implicit finite difference scheme and converted into a set of non-linear algebraic equations. The film equation Eq (31) was discretized with N_x non-uniform grid spacing along the gas-liquid interface, while Eq. (26) was solved with N_η grid points across the film. The following exponential form was used to generate non-uniform grid size at i-th point in the thickness and the transverse directions:

$$\Delta \eta(i) \equiv \frac{e^{-a(\frac{i-1}{N_\eta})} - e^{-a(\frac{i-2}{N_\eta})}}{e^{-a} - 1}, \tag{47}$$

$$\Delta x^*(i) \equiv \frac{e^{-\beta(\frac{i-1}{N_x})} - e^{-\beta(\frac{i-2}{N_x})}}{e^{-\beta} - 1}. \tag{48}$$

where α and β are the constants. The discretized diffusion model was solved by the implicit Tri-Diagonal-Matrix-Algorithm (TDMA) solver, while the time integrations for Eqs. (30)-(31) are fully explicit in the sense that the nonlinear h^2 and h^3 pre-factors and derivative terms are evaluated at the previous time level. The algebraic equations were solved with sufficiently small time steps of less than 7.8 μs to ensure the numerical stability. To find the unknown concentration fields at the next time step, the integrated concentration profile across the film, I_{cal}, was numerically obtained using Eq. (12), and the diagonal matrix was updated until the relative error holds $|(I - I_{cal})/I| < 10^{-6}$

where the integral I was calculated from Eqs. (13)-(14). Because of the steeper concentration gradient in the vicinity of the liquid-gas interface, the grid size of less than 58 nm was chosen to reduce the numerical errors.

The accuracy of the solutions was tested by decreasing the time interval and increasing the number of grid points in the thickness/transverse directions until the solutions converge. Furthermore, the preliminary computation for the poly(vinylacetate)-toluene liquid layer on a stationary substrate well reproduces the previous result for the residual solvent level [22], showing the validity of our numerical code. The detailed description of the code verification procedure is shown elsewhere [27].

RESULTS AND DISCUSSIONS

Stationary case

First, we present the simplest case where a single air jet impinges onto a liquid film on a stationary substrate, i.e., $\tau_w = \infty$. Figure 4 shows local variations in Bi number, surface tension, and wet film thickness as a function of the distance from the air impingement point. The solution was obtained for the initial film thickness of 300 μm, the polymer weight fraction of 9.98×10^{-3}, and the impinging air velocity of 10 m/s at the nozzle exit. The air blowing promotes two distinct regimes in Bi profiles: a flat plateau near the stagnation region and positive/negative gradients in the outer

15

regime (Figure 4a). The former corresponds to the cut-off heat/mass transfers in Eqs. (40) and (42), whereas does the latter to Eqs. (39) and (41) in the wall jet region. The resultant faster drying in the vicinity of the higher Bi plateau leads to a decrease in solvent concentration and thus a sharp drop in surface tension because of the solute surface activity (Figure 4b).

The non-uniform surface tension profile promotes the Marangoni stress, which drives the fluid from the air impingement region to the higher surface tension regions against capillary forces. As depicted in Figure 4c, the solution of the film equation shows a depression at the impingement point and convex crests in the outer regimes, indicating a particular drying-induced surface roughening. The axi-symmetric film evolution is qualitatively consistent with the previous modeling studies [17-20]. The computations also reveal that the surface elevation is significantly suppressed and eventually smoothed out with an increase in the viscosity power-law index. At the index of $\gamma=5$, the coating surface exhibits no particular elevations but rather shows a single depression, indicating the non-uniform thinning due to the faster film shrinkage in the stagnation regime.

To quantify the film evolution in detail, we defined the surface roughness, Δh, as the difference between the minimum thickness at the depression, h_{min}, and maximum thickness, h_{max}. Figure 5 shows the effect of impinging air velocity on the surface roughness for different viscosity indices. The roughness monotonically increases with the air velocity at the index factor of $\gamma=0$, i.e., in the case of constant viscosity $\mu=\mu_0$. In contrast, the calculated roughness first increases and then

decreases with an increase in velocity for higher viscosity fluids of $\gamma =1$ and 2. The increased fluid viscosity results in a lower critical air velocity at the peak.

The surface roughness variations with respect to the air velocity can be attributed to the balance between growing Marangoni stresses and competing shear forces that resist the surface deformation. An increase in air velocity leads to a steep surface tension gradient, which drives more fluids away from the impinging point to give higher surface ridges. On the other hand, a further increase in velocity leads to an exponential increase in surface viscosity. The resulting higher shear stress significantly retards the fluid motion and eventually immobilizes the coating surface at high air velocity regimes. Thus the coating no longer deforms even at steep surface tension gradients, leading to show a smoother surface at faster air impingements.

In order to support the description above, we obtained film equation solutions de-coupled from the surface-tension-driven transverse flow. The calculated de-coupled solutions of Eq. (6) are shown as the broken curves in Figures 4 and 5. Obviously, the coupled solutions converge to the de-coupled solution as increasing the fluid viscosity. The computation shows that the de-coupled solution profile in the x-direction exhibits a depression in the air stagnation regime, showing a quantitative agreement with that of coupled solution at $\gamma=5$. These facts suggest that the flow-induced surface roughness significantly reduces, whereas the depression due to the non-uniform thinning remains, as increasing the impinging air velocities and/or the fluid viscosities.

Moving case

We now consider how a moving coating exhibits dynamic responses to the Marangoni stress. Figure 6 presents one of the extreme cases when a liquid film is introduced into an impingement dryer at a constant speed of 1.0 m/s. The initial film thickness is 300 μm, and the impinging air velocity is 10 m/s. The time required for the web motion was chosen to be τ_w=100 ms by assuming the nozzle alignment with a regular spacing of 0.1 m. The sequential Bi peaks in Figure 6a correspond to the air stagnation points. The air blowing promotes a stepwise decrease in coating temperature, arising from the local evaporative cooling when the latent heat transfer overcomes the heat supplied from the air (Figure 6b). Interestingly, the computed solvent content reveals a particular growth/relaxation along the moving direction (Figure 6c), i.e., the normalized surface solvent concentration first drops at the first impingement point (I), increases in the region between two neighboring nozzles (II), and then decreases again as the coating approaches to the second impingement point (III).

The spatial concentration variation results in sequential spikes in the fluid viscosity (Figure 6d) and the surface tension (Figure 6e). The former tends to resist the transverse liquid motion, whereas the latter induces the Marangoni stress to drive the flow. As depicted in Figure 6f, the corresponding coating surface is found to exhibit the stress-induced roughening and the pressure-driven leveling in a sequential manner. The computation unambiguously shows that the growing surface topographies

are readily leveled in regimes between two neighboring nozzles. Furthermore, the local thickness on the moving web exhibits a ridge in upstream but no apparent ridge/depression in downstream, showing a particular asymmetric surface profile.

Figures 7a-7c demonstrate normalized solvent concentration profiles through the coating at three different drying times, corresponding to the points (I)-(III) in Figure 6c. When the coating passes just beneath the first nozzle, the solvent content drops near the interface to form a steep concentration gradient (Figure 7a). Deeper in coating, the concentration profile is still flat and keeps the initial value of unity. However, the concentration gradient is significantly relaxed at the point (II) where the coating locates in the lower Bi regime (Figure 7b). A further drying to the point (III) leads to a re-development of a steeper concentration gradient (Figure 7c). These facts suggest that the periodic air blowing locally disrupts the subtle balance of mass transfer rates across the gas/liquid interface, giving rise to the growth and relaxation in the concentration profiles across the film. Note that the previous drying models using spatially-uniform Biot numbers are hopeless to predict such a relaxation in the concentration field.

To address the unique surface evolution on the moving coating, we first estimated the time scales required for the growth/decay in surface topography. Using the long-wave approximation, the time scales for the Marangoni and leveling flows are respectively given by $\tau_m = \mu /(\Delta\sigma B_i k^2 L)$ and $\tau_l = 3\mu /(\sigma L^3 k^4)$. Substituting typical computational values of L=300 μm, μ=2 mPa·s, σ =67mN/m, Δσ

=0.05mN/m, B_i=150, and k=500 m^{-1} corresponding to the case in Figures 6 and 7 yields the relevant

time scales as τ_m=4 ms and τ_l=50 ms. Thus the shorter surface evolution times compared to that of

web motion (τ_m/τ_w ~0.04) allow the surface to respond to local stress variations in a finite time

before the coating moves to the neighboring nozzle.   This is consistent with the sequential growth

in the surface topography shown in Figure 6f.

The above estimate also implies that the stress-induced roughening is readily followed by the

leveling when the surface tension gradient relaxes. Let us consider a surface spot locating upstream

from an air-impingement point. As the coating approaches to the point, the local surface tension

gradient, and thus the interfacial stress, increases to induce crests and a depression as does for the

stationary case. However, the downstream stress begins to reduce in magnitude after the coating

passes through the point and eventually becomes too small to promote the liquid motion. Thus the

opposing leveling flow becomes dominant and tends to decay the downstream topographies when τ_l

$/\tau_w$<1. Indeed, this argument is consistent with the asymmetric surface evolution shown in Figures 6f.

In contrast, the growing topographies might not decay but rather remain on the coating surface in the

opposing case of $\tau_l \gg \tau_w$.

If the time scale for the web motion becomes shorter than those for the surface deformation (τ_m

$/\tau_w$ >1), then the coating passes through the impingement point before it responds to the interfacial

stress. Thus we expect a smooth surface topography at high web speeds. To verify this hypothesis,

the surface evolution was examined as a function of the web speed. Figure 8 presents the local

distribution of the wet thickness in the vicinity of 0.5 m downstream from the dryer inlet. The web

speed ranged between 0.2 and 10 m/s, corresponding to the time scales of web motion of τ_w =500 ms

−10 ms. The surface evolution time scale via the Marangoni stress was estimated using the

long-wave approximation and found to be τ_m=40 ms . When τ_m / τ_w ~0.1 at the web speed of 0.2 m/s,

the surface was found to exhibit the noticeable elevation in upstream and the broad depression and

the crest (a half portion is shown) in downstream. In contrast, these topographies tend to decay as

increasing the web speed, and finally diminish in the range of web speeds above 10 m/s for τ_m / τ_w >

1.

The similar trend was observed when we increase the liquid viscosity, while the web speed is kept

constant. Figure 9 shows solutions of the film equation for three different viscosity power-law

indices at a given time scale of τ_w =500 ms. An increase in viscosity index results in a significantly

reduced surface roughness with less elevation. The surface viscosity in the vicinity of the air

impingement point was found to rise from 1.4 mPa· s upto 16 mPa· s as increasing the index from

γ=1 to 3. The corresponding time scale obtained from the long wave approximation increases from

τ_m =40 ms to 500 ms, suggesting that the surface evolution time scale becomes comparable to that of

the web motion at γ=3. Thus the moving surface no longer involves enough time to respond to the

local stress, resulting in smoothed surface profiles in a particular range of time scales.

21

Figure 10 depicts the variations in surface roughness with the web speed, corresponding to the

case in Figure 8. For some cases when no apparent surface depression was observed, we determined

the critical x-coordinate x_c, at which the second derivative d^2h/dx^2 shows a maximum peak, and $h(x_c)$

was taken as the local minimum thickness. The computations reveals that the calculated roughness

reduces by orders of magnitude with an increase in the web speed, showing unambiguous evidence

that the coating operations faster than the film evolution significantly retards the surface roughening.

The drying-induced surface roughness can also be tuned when the impinging air velocity is varied.

Figure 11 presents drying maps to show how the roughness varies with the air velocity and the web

speed at a point 0.5 m downstream from the dryer inlet. The smoother coating surface is obtained at

lower air velocities and higher web speeds. Reducing the web speed at a given air velocity leads to a

drastic increase in surface roughness for the low viscosity fluid of $\gamma=1$ (Figure 11a). For the fluid of

$\gamma=2$ with stronger concentration-dependence on viscosity (Figure 11b), the surface roughness is

significantly retarded in whole drying map regimes, because of the suppressed transverse fluid

motion via higher shear stresses. These facts suggest that not only the operating variables but also

the rheological behaviors of coating liquids play a key role in the optimal design of the air

impingement drying process.

We should note that the heat conduction and the mass transport in the transverse direction are

simply neglected in the computations described here, which may overestimate the transverse

22

gradients in the temperature/concentration and thus the interfacial stress. Furthermore, the neglected air-jet shear stresses may limit the present model to a particular range of air velocities. Nevertheless, our model could form the basis for the fundamental understanding of how the coating responds to the local variations in drying-induces stresses in industrial air blowing operations. More detailed validation including a quantitative comparison with experiments as well as a model extension to three-dimensional systems would be the subject of future research.

CONCLUSIONS

We present a drying model of binary solution coatings that respond to periodic variations in Marangoni stresses. The model enables us to simulate the growth and relaxation in the concentration gradient, and thus the interfacial stress, as the coating moves beneath air-blowing nozzle arrays. The transverse lubrication flow driven by the surface-tension-gradient is coupled with one-dimensional mass/heat transfers across the coating to predict the surface deformation in early evaporation stages. Numerical computations reveal that moving coatings exhibit asymmetric thickness variations that grow and level in a sequential manner. The properly chosen operating conditions significantly suppress the drying-induced surface roughening, depending on the time scales of the surface evolution and the substrate motion.

Literatures Cited

1. Oron A, Davis SH, Bankoff, SG, Long-sale evolution of thin liquid films. *Reviews of Modern*

    Physics. 1997;69:931-980.

2. Cairncross RA, Jeyadev S, Dunham RF, Evans K, Francis LF, Scriven LE, Modeling and design

    of an industrial dryer with convective and radiant heating. *Journal of Applied Polymer Science*.

    1995;58:1279-1290.

3. Aust R, Durst F, Raszillier H, Modeling a multiple-zone air impingement dryer. *Chemical*

    Engineering and Processing. 1997;36:469-487.

4. Barttfeld M, Alleborn N., Durst F., Dynamic optimization of multiple-zone air impingement

    drying processes, *Computers and Chemical Engineering*. 2006;30:467-489

5. Guerrier B, Bouchard C, Allain C, Benard C, Drying kinetics of polymer films. *AIChE Journal*.

    1998;44:791-798.

6. Price PE Jr, Cairncross RA, Optimization of single-zone drying of polymer solution coatings to

    avoid blister defects. *Drying Technology*. 1999;17:1303-1311.

7. Wong SS, Altinkaya SA, Mallapragada SK, Drying of semicrystalline polymers: mathematical modeling and experimental characterization of poly(vinyl alcohol) films. *Polymer*. 2004;45:5151-5161.

8. Wong SS, Altinkaya SA, Mallapragada SK, Crystallization of poly(vinyl alcohol) during solvent removal: infrared characterization and mathematical modeling. *Journal of Polymer Science: Part B: Polymer Physics*. 2007;45:930-935.

9. Cairncross RA, Francis LF, Scriven LE, Predicting drying in coatings that react and gel:drying regime maps. *AIChE Journal*. 1996;42:55-67.

10. Alsoy S, Duda JL, Influence of swelling and diffusion-induced convection on polymer sorption processes. *AIChE Journal.* 2002;48:1849-1855.

11. Vinjamur M, Cairncross RA, Non-Fickian nonisothermal model for drying of polymer coatings. *AIChE Journal*. 2002;48:2444-2458.

12. Okuzono T, Ozawa K, Doi M, Simple model of skin formation caused by solvent evaporation in polymer solutions. *Physical Review Letters*. 2006;97:136103-1-136103-4.

13. Yamamura M, Uchinomiya T, Mawatari Y, Kage H, Aymmetric surface roughness formation on moving non-isothermal liquid coatings. *International Polymer Processing*. 2007;12:1-5.

14. Gramlich CM, Kalliadasis S, Homsy GM, Messer C, Optimal leveling of flow over one-dimensional topography by Marangoni stresses. *Physics of Fluids*. 2002;14:1841-1850.

15. Yiantsios SG, Higgins B, Marangoni flows during drying of colloidal films. *Physics of Fluids*. 2006;18:082103-1-082103-11.

16. Eres MH, Weidner DE, Schwartz LW, Three-dimensional direct numerical simulation of surface-tension-gradient effects on the leveling of an evaporating multicomponent fluid. *Langmuir.* 1999;15:1859-1871.

17. Evans PL, Schwartz LW, Roy RV, A mathematical model for crater defect formation in a drying paint layer. *Journal of Colloid and Interface Science*. 2000;227:191-205.

18. Schwartz LW. Roy RV, Eley RR, Petrash S, Dewetting patterns in a drying liquid film. *Journal of Colloid and Interface Science*. 2001;234:363-374.

19. Blunk RHJ, Wikes JO, Computational analysis of surface-tension-driven coating-defect flow. *AIChE Journal*. 2001;47:779-789.

20. Edmonstone BD, Matar OK, Simultaneous thermal and surfactant-induced Marangoni effects in thin liquid films. *Journal of Colloid and Interface Science*. 20014;274:183-199.

21. Vrentas JS, Vrentas CM, Drying of solvent-coated polymer films. *Journal of Polymer Science: Part B: Polymer Physics*. 1994;32:187-194.

22. Alsoy S, Duda L, Drying of solvent coated polymer films. *Drying Technology.* 1998;16:15-44.

23. Martin H, Heat and mass transfer between impinging gas jets and solid surfaces. *Advances in heat transfer.* (1977);13:1-60.

24. Kumada M, Nakatogawa T, Hirata L, *Journal of the Japan Society of Mechanical Engineers.* (in Japanese) 1973:76:12-20.

25. Zielinski JM, Duda JL, Predicting Polymer/Solvent Diffusion Coefficients Using Free-Volume Theory. *AIChE Journal*. 1992;38:405-415.

26. Okazaki M, Shioda K, Masuda K, Toei R, Drying mechanism of coated film of polymer solution. *Journal of Chemical Engineering of Japan*. 1974:7:99-105.

27. Yamamura M, Mawatari Y, Kage H, submitted

LIST OF FIGURES

gas-solution interface, (d) surface solution viscosity, (e) surface tension, and (f) coating thickness distributions on a substrate moving at U=1 m/s. The solvent content reveals a particular growth/relaxation along the moving direction, resulting in a sequential stress-induced roughening and pressure-driven leveling. The initial film thickness is 300 μm, the viscosity power-law index is γ =1, and the impinging air velocity is 10 m/s.

Figure 7   Normalized solvent concentration profiles at three different drying times, corresponding to the points (I)-(III) in Figure 6c. The periodic air blowing gives rise to the growth and relaxation in the concentration profiles across the film.

Figure 8   Variations in the local wet thickness at four different web speeds in the vicinity of 0.5 m downstream from the dryer inlet. The surface topographies decay as increasing the web speed and finally diminish at the web speeds of 10 m/s. The initial film thickness is 300 μm, the viscosity power-law index is γ =1, and the impinging air velocity is 1 m/s.

Figure 9   Variations in the local wet thickness at three different viscosity power-law indices. An increase in viscosity index results in a significantly reduced surface roughness with less elevation. The initial film thickness is 300 μm, the web speed is U=0.2 m/s, and the impinging air velocity is 1 m/s.

Figure 10 Variations in surface roughness with the web speed, corresponding to the case in Figure 8. The calculated roughness reduces by orders of magnitude with an increase in the web

speed.

Figure 11 Drying regime maps showing surface roughness calculated at a point 0.5 m downstream

from the dryer inlet as functions of the impinging air velocity and the web speed for (a)

γ =1 and (b) γ =2. The smoother coating surface is obtained at low air velocity and high

web speed regimes. The initial film thickness is 300 μm.
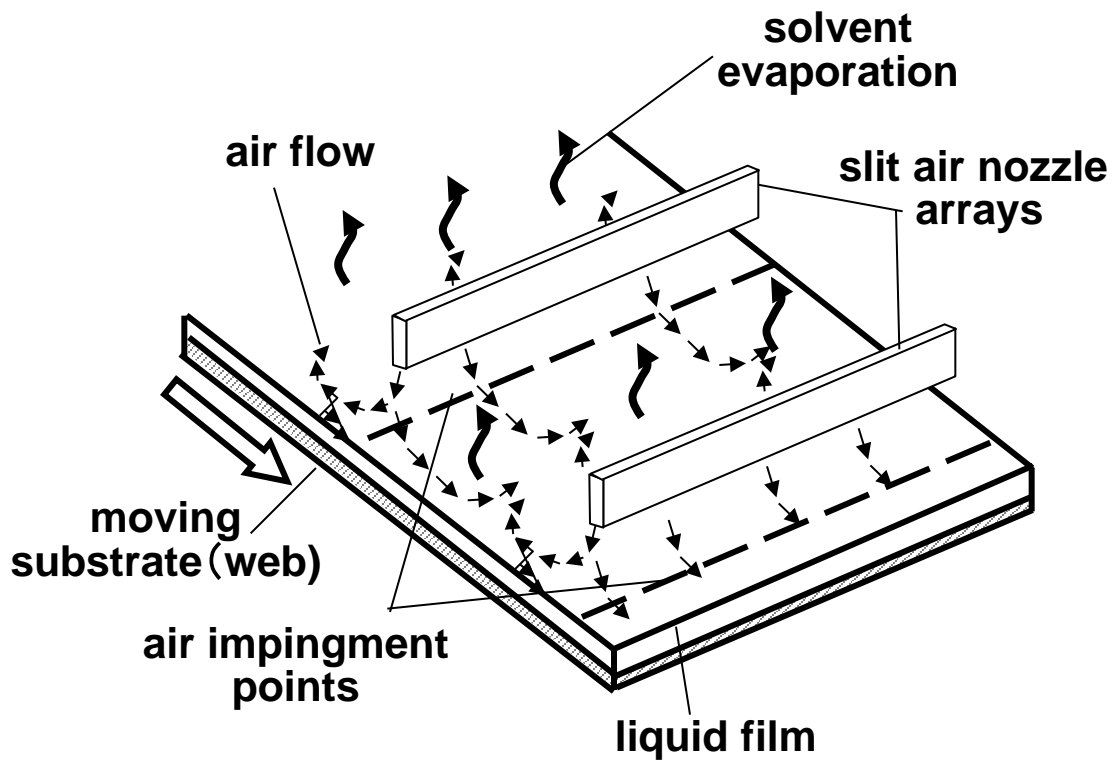
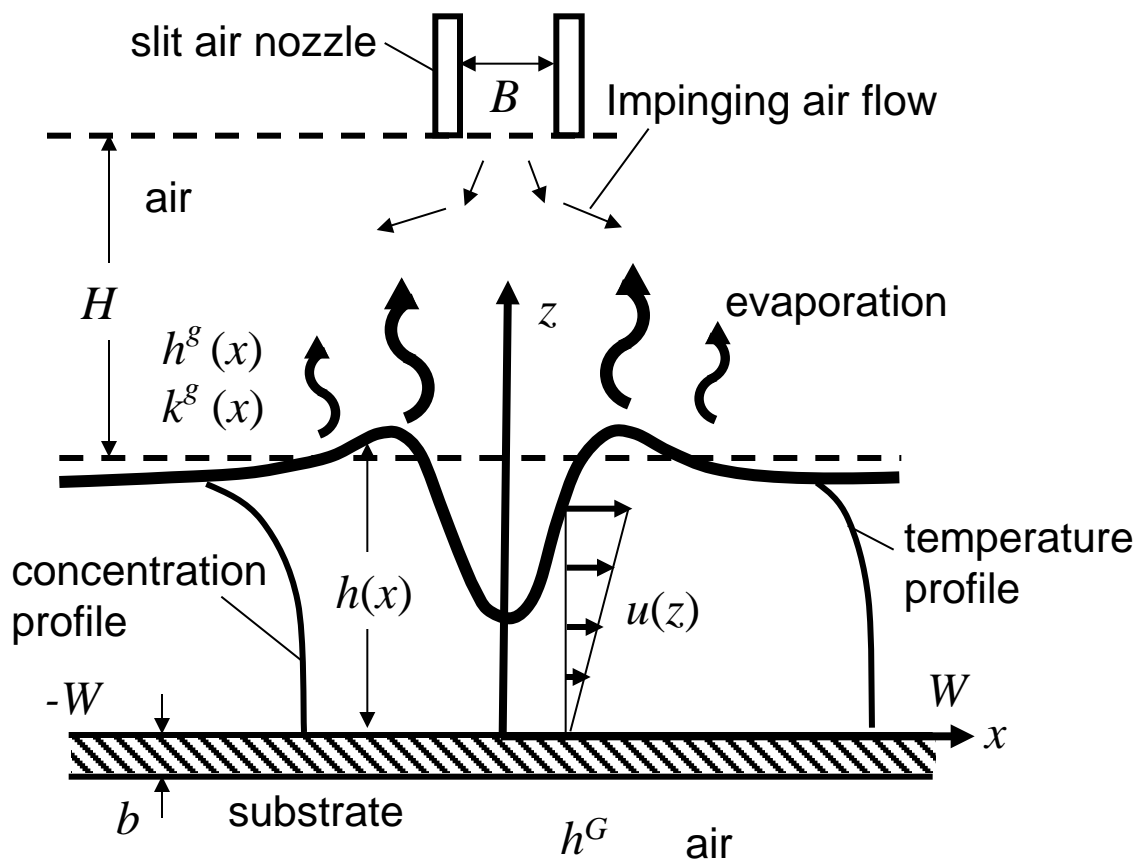Figure 1 Coated film on a moving web subjected to periodic air blowing from slit nozzles.
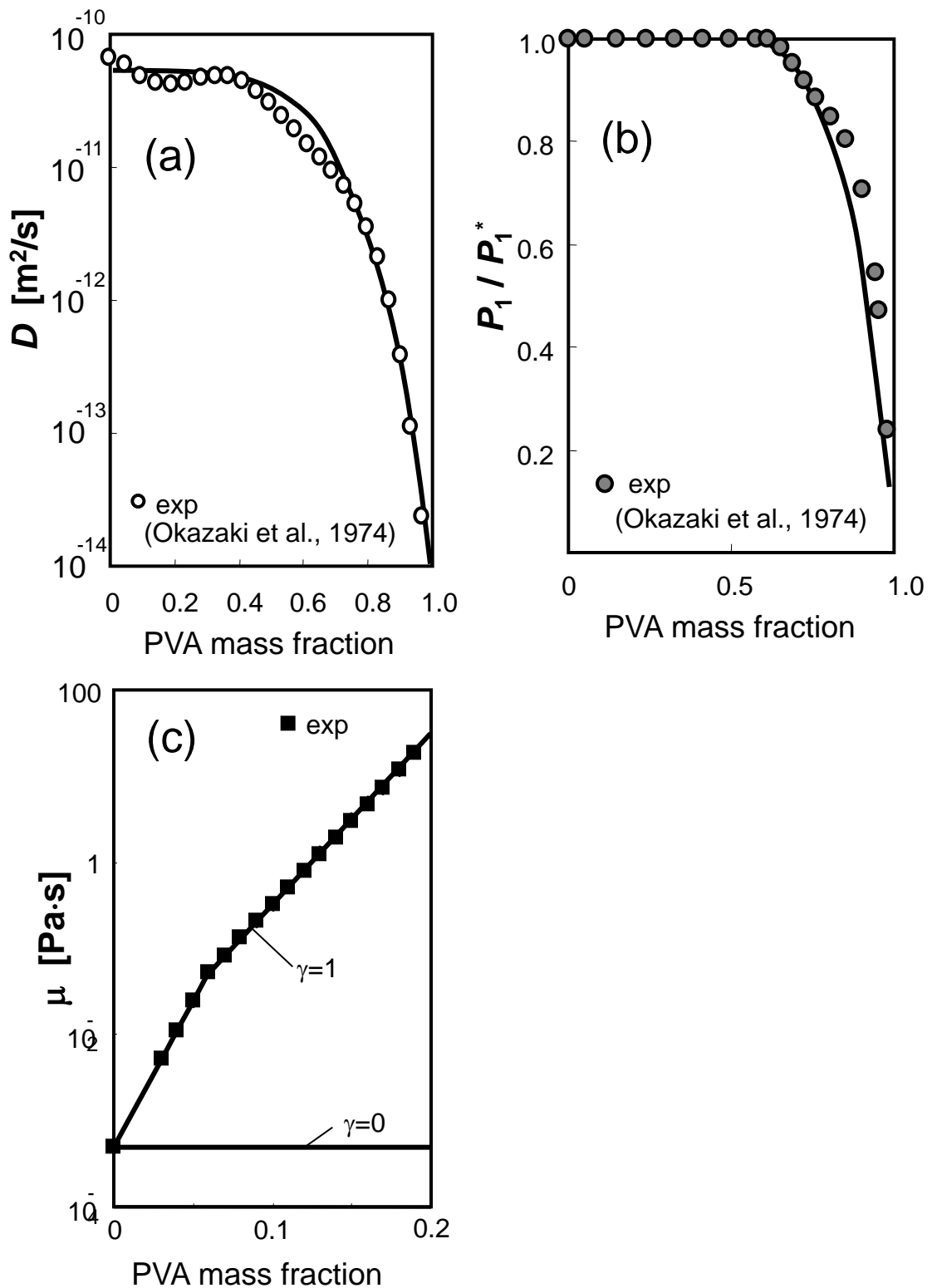
Figure 2 Drying geometry in a unit computational cell.

Figure 3 (a) Mutual diffusion coefficient, (b) saturated vapor pressure, and (c) liquid viscosity of poly(vinyl-alcohol)(PVA)/water binary solution as a function of PVA mass fraction. The solid curves represent the correlated values used in the computation.

Table 1 Typical parameter values of polyvinyl alcohol solution drying. *Determined by fitting Equations (45)-(47) with experimental data from Okazaki et al. [26].

gas parameters

$P_{1b} = 2190$ Pa

$\rho^G = 1.0315$ kg/m^3

$\mu^G = 1.970 \times 10^{-5}$ Pa·s

$C_p^{\ G} = 1.018 \times 10^3$ J/(kg·K)

$\lambda^G = 0.02618$ J/(m·s·K)

$M_1 = 18$ g/mol

$D^G = 3.20 \times 10^{-5}$ m^2/s

substrate parameters

$h_s = 100 \mu$m

$\rho_s = 1270$ kg/m^3

$\lambda_s = 0.400$ J/(m·s·K)

$C_{Ps} = 1.25 \times 10^3$ J/(kg·K)

drying conditions

$L = 300$ μm

$B = 0.005$ m

$H = 0.05$ m

$W = 0.05$ m

$u^G = 10$ m/s

$U = 1.0$ m/s

$T_0 = 330$ K

$T_b = 350$ K

$h^G = 500$ J/(m^2·s·K)

solution parameters

$\chi_{12} = 0.80^*$

$\rho_0 = 1000$ kg/m^3

$\rho_{10} = 992$ kg/m^3

$\tilde{V}_1 = 1.00 \times 10^{-3}$ m^3/kg

$\tilde{V}_2 = 8.00 \times 10^{-4}$ m^3/kg

$C_p = 4.18 \times 10^3$ J/(kg·K)

$\Delta H = 2261$ kJ/kg

$\lambda = 0.657$ J/(m·s·K)

$\sigma_T = -1.396 \times 10^{-4}$ N/(m·K)

$\sigma_c = 3.48 \times 10^{-5}$ m^3/s^2

$\sigma_0 = 0.07275$ N/m

$D_0 = 2.0 \times 10^{-10}$ m^2/s

$D_{10} = 5.0 \times 10^{-11}$ m^2/s*

$m_D = 9^*$

$n_D = 5^*$

$\mu_0 = 0.4899$ mPa·s

$m_\mu = 0.778 \times 10^{-2}$ ($\rho_1 / \rho_{10} \leq 0.06$)

$m_\mu = 0.449 \times 10^{-2}$ ($\rho_1 / \rho_{10} \geq 0.06$)

$n_\mu = 1970$ K

$k_\mu = -5.97$ ($\rho_1 / \rho_{10} \leq 0.06$)

$k_\mu = -3.99$ ($\rho_1 / \rho_{10} \geq 0.06$)

computation parameters

$\alpha = 6$
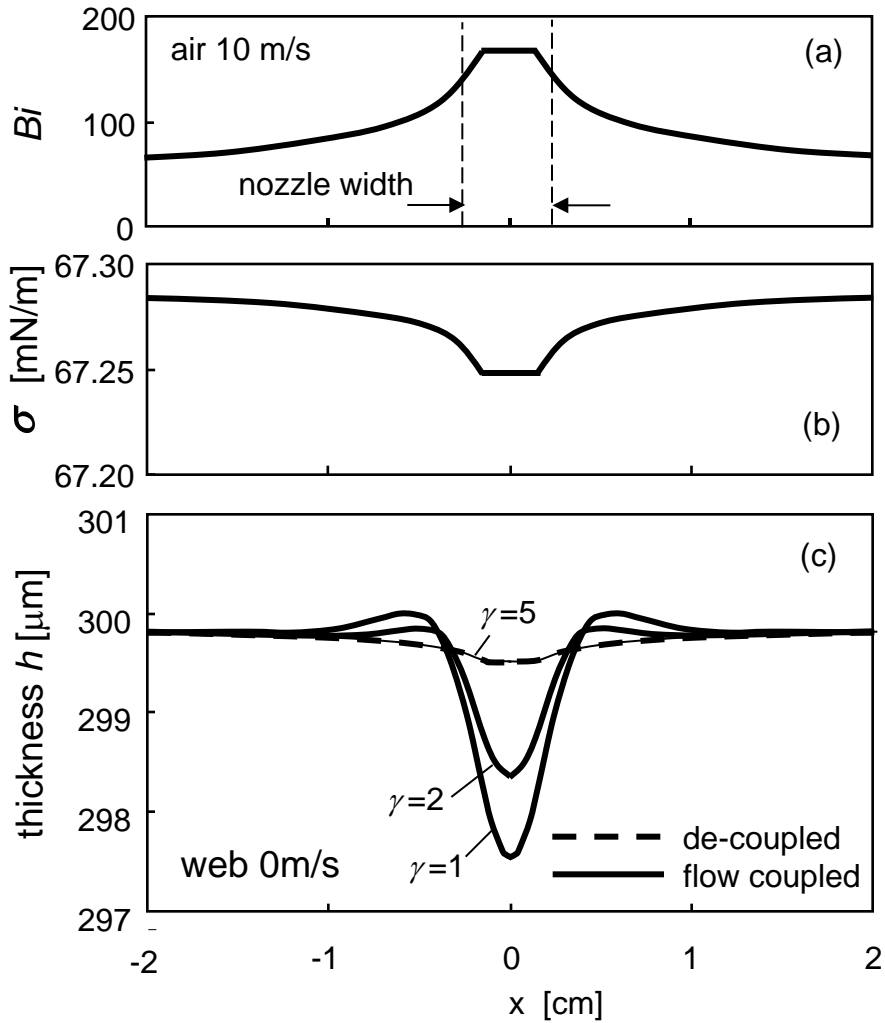
$\beta = 3$

$N_\eta = 80$

$N_x = 20$

Figure 4 (a) Biot number, (b) surface tension, and (c) coating thickness distributions on a stationary substrate at *t*=0.03 s. The non-uniform surface tension profile drives the fluid from the air impingement region and promotes drying-induced surface ridges. The initial film thickness is 300 μm, the polymer weight fraction is 9.98×10⁻³, the nozzle width is 5 mm, and the impinging air velocity is 10 m/s at the nozzle exit.
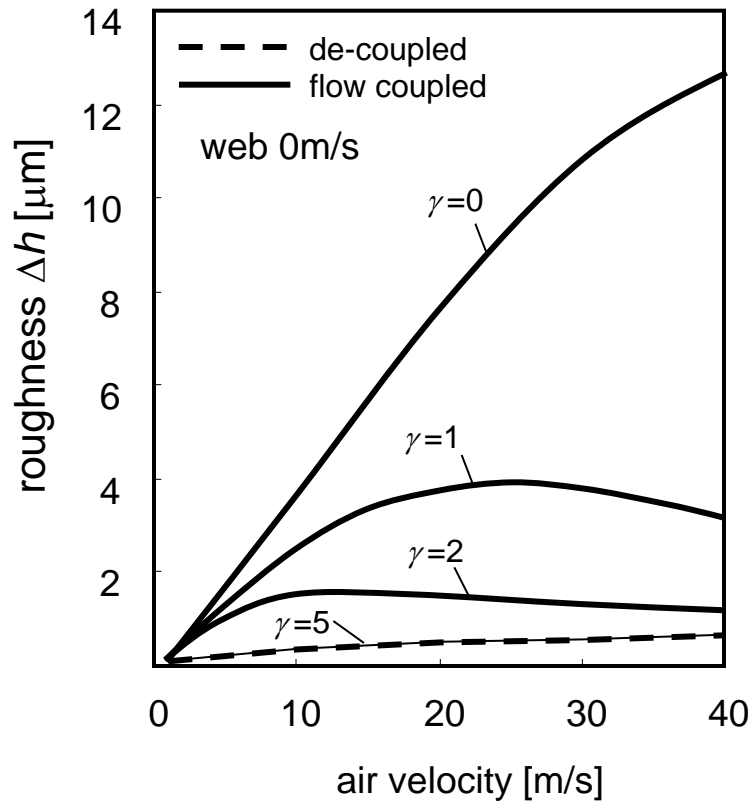
Figure 5 The effects of impinging air velocity on the surface roughness on a stationary web at the elapsed drying time of 0.03 s, corresponding to the computational conditions in Figure 4. The calculated roughness first increases and then decreases with an increase in velocity for $\gamma =1$ and 2. The solutions converge to the de-coupled solution (broken curve) at $\gamma =5$.
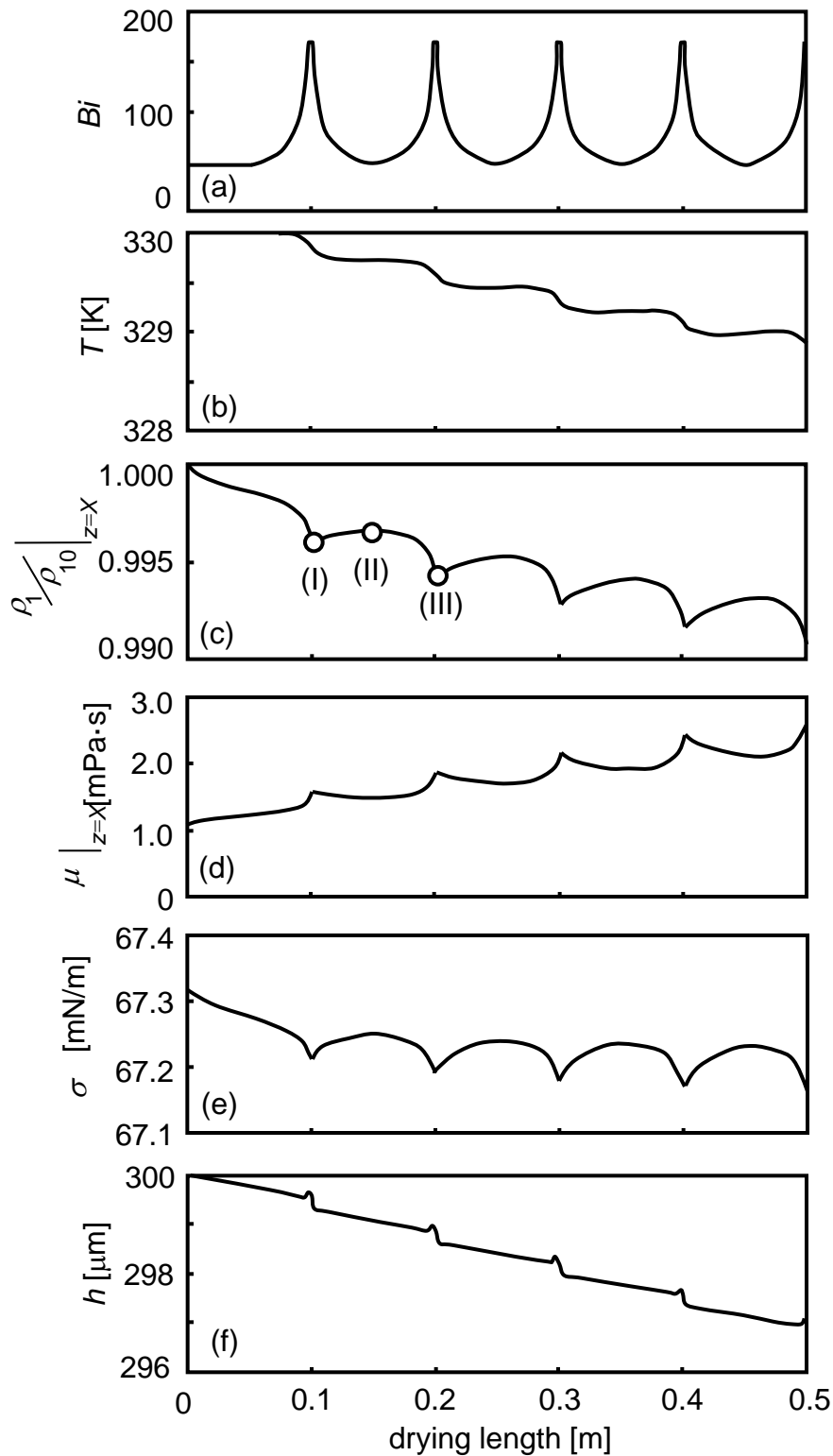
Figure 6 (a) Biot number, (b) temperature, (c) normalized solvent mass concentration at gas-solution interface, (d) surface solution viscosity, (e) surface tension, and (f) coating thickness distributions on a substrate moving at U=1 m/s. The solvent content reveals a particular growth/relaxation along the moving direction, resulting in a sequential stress-induced roughening and pressure-driven leveling. The initial film thickness is 300 μm, the viscosity power-law index is $γ$ =1, and the impinging air velocity is 10 m/s.

Figure 7 Normalized solvent concentration profiles at three different drying times, corresponding to the points (I)-(III) in Figure 6c. The periodic air blowing gives rise to the growth and relaxation in the concentration profiles across the film.
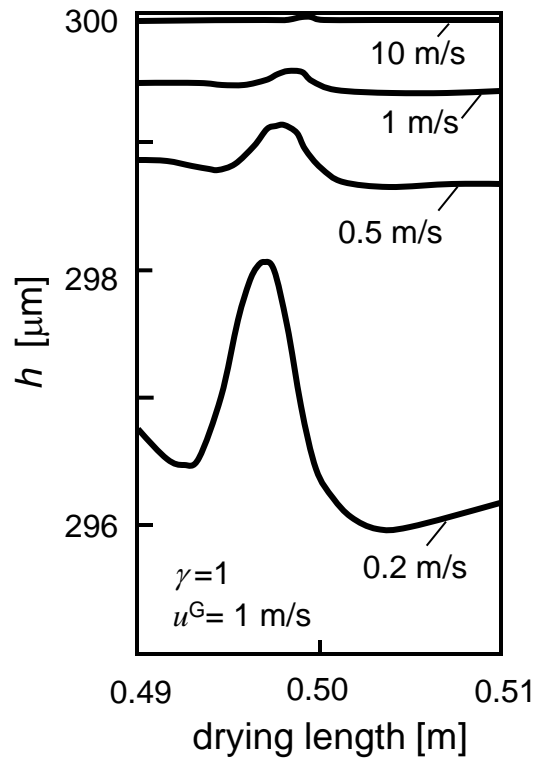
Figure 8 Variations in the local wet thickness at four different web speeds in the vicinity of 0.5 m downstream from the dryer inlet. The surface topographies decay as increasing the web speed and finally diminish at the web speeds of 10 m/s. The initial film thickness is 300 μm, the viscosity power-law index is $\gamma = 1$, and the impinging air velocity is 1 m/s.
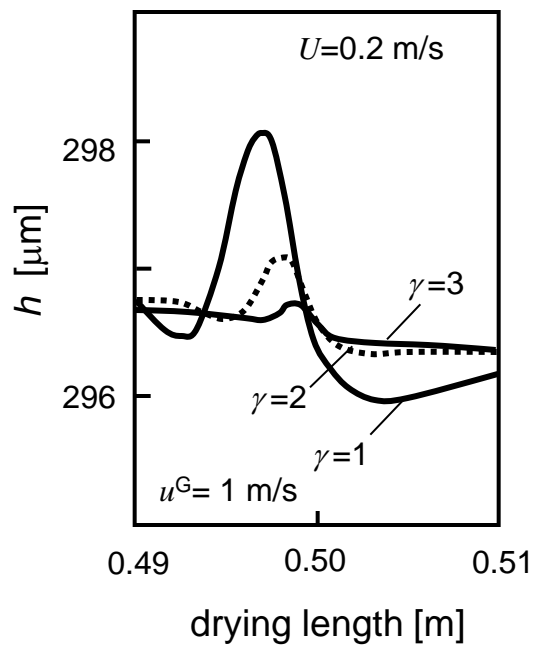
Figure 9 Variations in the local wet thickness at three different viscosity power-law indices. An increase in viscosity index results in a significantly reduced surface roughness with less elevation. The initial film thickness is 300 μm, the web speed is U=0.2 m/s, and the impinging air velocity is 1 m/s.
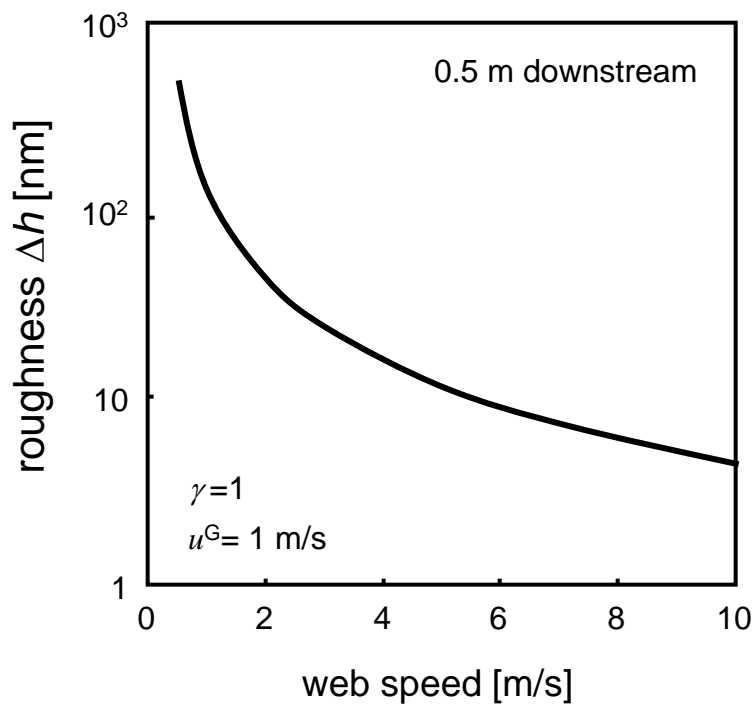
Figure 10 Variations in surface roughness with the web speed, corresponding to the case in Figure 8. The calculated roughness reduces by orders of magnitude with an increase in the web speed.
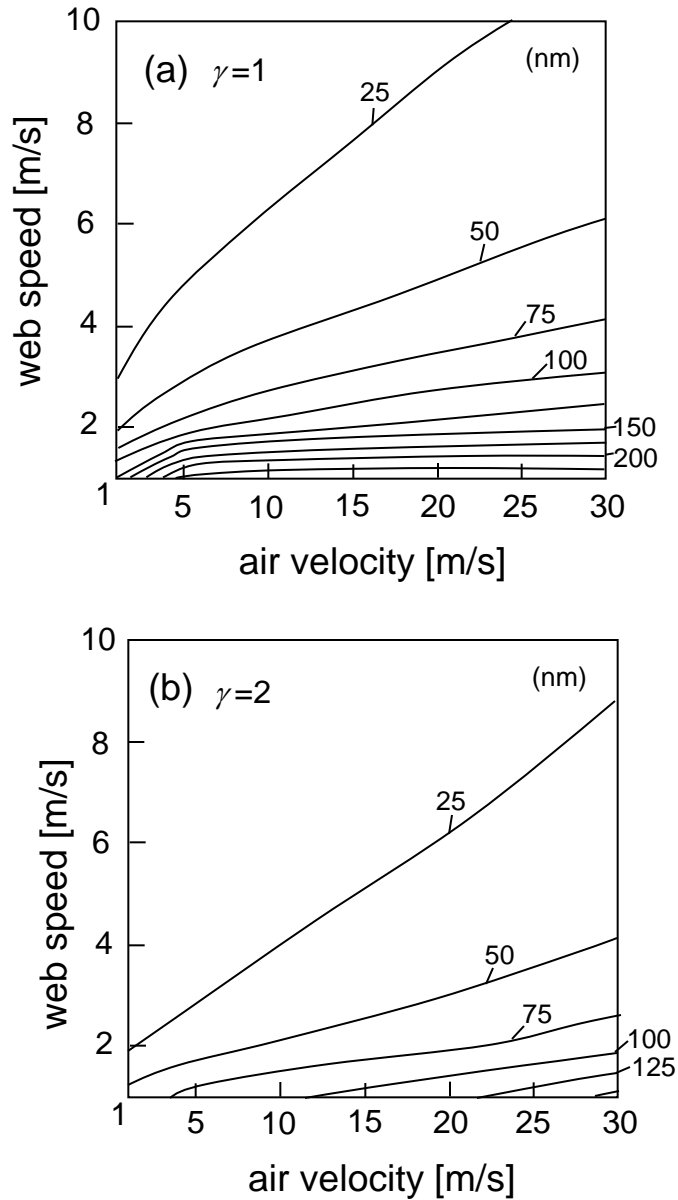
Figure 11 Drying regime maps showing surface roughnesses calculated at a point 0.5 m downstream from the dryer inlet as functions of the impinging air velocity and the web speed for (a) γ =1 and (b) γ =2. The smoother coating surface is obtained at low air velocity and high web speed regimes. The initial film thickness is 300 μm.